energies

MDPI

Article

CFD Prediction of a Double Impulse Burner for Glass Furnaces

Carlo Cravero, Alessandro Lamberti * and Luca Poggio

Dipartimento di Ingegneria Meccanica, Università degli Studi di Genova, 16145 Genoa, Italy; cravero@unige.it (C.C.); luca.poggio98@gmail.com (L.P.)
* Correspondence: alessandro.lamberti@edu.unige.it

Abstract: Recently, growing environmental awareness has radically changed the way the problems and priorities of industry are dealt with. Energy issues have become an issue of primary importance, both in terms of consumption and polluting emissions. However, for the green transition to happen, the first step is to have a deeper knowledge of the phenomena involved in processes with a special focus on combustion. The glass industry is one of the most energy-intensive since a temperature of over 1400 °C is required to keep glass molten, with a large consumption of natural gas used for combustion. A fundamental element to control the process is the burner. In this study, the CFD (Computational Fluid Dynamics) prediction of the internal streams repartition and the velocity profile at the exit, at different geometrical setups and operating conditions, of an industrial burner for glass furnaces is presented, with the aim of developing a surrogate model to provide these two important quantities quickly. The study of the repartition of the mass flow inside a double impulse burner and the subsequential velocity profile outside the burner is a novelty in the glass industry. The CFD prediction of the operating conditions is a crucial aspect because it is an essential boundary condition for the simulation of the reactive process from the diffusive flame found in glass furnaces. Different operating and geometrical conditions of the burner have been tested using Ansys CFX code, and results (velocity profile and mass flow repartition) have been organized in surrogate models. Results showed that the repartition of the fuel streams is mainly influenced by the position of the barrel, while the total flow rate is strongly influenced by the total inlet pressure. The internal flow varies from 20% to 50% of the total mass flow inside the burner, while the velocity magnitude outside the burner varies from 80 to 300 m/s approximately. The reconstruction of velocity profiles at the exit of the burners with surrogate models showed an acceptable match with numerical simulations.

Keywords: double impulse burner; CFD; glass furnace; surrogate model; response surface method (RSM)

Citation: Cravero, C.; Lamberti, A.; Poggio, L. CFD Prediction of a Double Impulse Burner for Glass Furnaces. *Energies* **2023**, *16*, 4275. https://doi.org/10.3390/en16114275

Academic Editors: Maryam Ghodrat and Enrico Nobile

Received: 28 March 2023
Revised: 13 May 2023
Accepted: 17 May 2023
Published: 23 May 2023

1. Introduction

Flow inside the fuel burner and the resulting flame in a furnace is a crucial field of research to reduce carbon and NOx emissions by the glass industry.

The profile and the magnitude of velocity outside the burner are relevant for the formation of pollutants because of the length and the shape of the developed diffusive flame. One of the keys to the success of new technology is the capability to design new types of burners, requiring an adequate physical understanding of the phenomena associated with new geometry and different working fuels.

Several CFD solutions for glass furnaces burners can be found in the literature: Simpson [1] performed several experiments to establish the connection between the NOx formation and the heat transfer inside the glass furnace. He found that if there is low NOx emission, the resulting heat transfer is higher. By sealing burners and using either dual impulse or multi-hole burners, there can be a significant reduction in NOx with a corresponding increase in heat transfer. An increase in heat transfer lowers energy, CO_2, and total emissions resulting in smaller post-treatment abatement devices and lower operating costs. Korstanje et al. [2] carried out tests to study the NOx emission and heat transfer of burners for regenerative

glass melting furnaces. The performance of "single hole" natural gas burners was investigated, and two more complex "low NOx" natural gas burners were tested. The results show that with proper changes in the design and operation of burners used in glass furnaces, it is possible to reduce the NOx emission and simultaneously increase the heat transfer. Nakamura et al. [3] experimentally investigated novel NOx-reduction methods and their impact on heat transfer in glass-melting furnaces fired by natural gas. Results suggested a few practical NOx-reduction techniques applicable to high-temperature furnaces. It has been demonstrated that by optimizing the mixing of fuel and air, a significant reduction in NOx is achievable while maintaining thermal efficiency and heat-transfer characteristics within acceptable limits. The fuel-efficiency levels varied between 49% and 55% of the fuel input, dependent on the firing mode. Heat transfer is also shown to be better when the temperature field is uniform, so the heat transfer to the glass is higher. Liu et al. [4] provided 3D numerical simulations to improve the geometrical parameters of a fuel-staged low NOx gas burner. The primary gas injection angle, the staged gas injection angle, and the position of the staged gun were adapted based on the NO emission and the chemical flame size. Overall, they found optimal geometrical parameters from the point of view of Nox emissions, flame size, and industrial limitations. Guihua et al. [5] carried out CFD simulations, including flow patterns, combustion, and heat transfer in a cracking furnace. Zhou et al. [6] summarized the results of a study of a low-NO_X burner for coal-fired boilers. Their study was focused on validating the CFD predictions on NO_X emission against a single burner full-scale experimental measurement. A numerical study by Khazaei et al. [7] investigates the effects of using a diluted fuel in an industrial furnace under several cases of conventional and highly preheated and diluted air combustion conditions working with a self-made computer code. A study by Khazaei et al. [8] shows the modeling and simulation of an industrial furnace under conventional combustion as well as under highly preheated and diluted air combustion (HPDAC) conditions. The authors wrote FORTRAN code and performed simulations using it. Bao et al. [9] simulated the combustion distribution in a burner, which showed how the combustion is distributed in the burner after optimizing the internal layout. In a study by Chen et al. [10], they validated the Low-NO_x strategy of the folded flame pattern based on a fuel-staging natural gas burner. Mei et al. [11] designed and numerically simulated an oil-fired oxy-fuel glass furnace. They developed an optimization path by testing two burner solutions, opposed or staggered. By comparing the flow fields in the opposed and staggered burner arrangements, they state that it is better to choose the burners in a staggered manner for the design furnace because the temperature is uniform, and the flow field is favorable and beneficial for decreasing the crown heat duty; the resulting heat transfer rate to the liquid glass surface is higher. Choudhary [12] has shown significant developments in the mathematical modeling of flow and heat transfer in glass furnaces in recent years. He described advances in the fundamental scientific and practical aspects of modeling. The most effective technology to tackle the innovation process in this industrial problem is to make intensive use of numerical simulations properly tuned for the difficult case of reactive flow with diffusive flames in a hot stream of air. The first part of this study is related to the development of two coaxial jets because it is the underlying mechanism inside the double impulse burner. Franchina et al. [13] addressed the problem of coaxial jets in a non-reacting mixture of fuel and air. Their work deals with the development of an original Discontinuous Galerkin (DG) finite element method and its application to computing non-reactive aerodynamics in multicomponent gaseous mixtures in turbulent regime, tested against various experimental data, performing comparisons with the outputs of a commercial code. The proposed DG code performs well, and the results agree with the measurements. They found that, with reference to the commercial code, their FEM (Finite Element Method) code is closer to experimental data. Villermaux et al. [14] studied the minimum set of ingredients required to understand the progress of the mixing process in a prototype shear flow. Their work suggests that the only two quantities necessary to understand the main phenomena of mixing are the initial vorticity thickness, set by the initial Reynolds number, and the elongation rate constructed

with the net velocity difference between the streams and the gap width. Behrouzi et al. [15] carried out an experimental study to show the effect of coaxial nozzle operating conditions on the development of the jet plume. They say that the coaxial jet flow development primarily depends on the combination of nozzle pressure ratios between the inner and outer zone.

The main part of the present work is than focused on an industrial burner for glass furnaces. The effects of variation in geometric parameters and inlet mass flow of the swirler were examined in a study by Khandelwal et al. [16]. Yang et al. [17] numerically studied the combustion of a single jet of propane in a cross-flowing stream of preheated and oxygen-deficient air with an emphasis on the influence of fuel temperature.

The study of two glass-melting furnaces is presented by Falcitelli et al. [18]. They experimentally tested some furnaces and then performed CFD simulations, adopting suitable boundary conditions for the radiative heat exchange and the chemical reaction kinetics. Galletti et al. [19] presented a 3D CFD model of the burner and compared it to an axisymmetric model, which saves considerable computational time but does not allow for considering some important burner characteristics, such as the presence of recirculation zones. This present study is a contribution to this research goal, and it is focused on modeling a double impulse burner (frequently used in glass furnaces) with a dual objective: to develop a surrogate model to support the operation of the burner and to set up a model for the velocity profile at the outlet section. This is a crucial aspect as a boundary condition for reactive flows in diffusive flame development and has not been specifically studied in the existing literature. Indeed, in this present study, several numerical simulations of different operating conditions of a burner (that would result in many hours of experimental processes and a large amount of fuel consumption, and possible large wasted production) have been performed. The novelty of this study is the methodology developed based on specific post-processing of the numerical results and the setup of surrogate models to support the operation of the burner. Results from numerical simulations have been analyzed with an Artificial Neural Network and other response surface methods to obtain different correlations for the repartition of the flow streams inside the burner and to obtain a model for the velocity profiles at the burner exit that are crucial for the diffusive flame development.

2. The Double Impulse Burner

The first aspect was the development of a 3D CAD model for the burner that has been available from an industrial partner as a physical part. The burner has been disassembled, as shown in Figure 1, then each part has been measured. The 2D drawings of each component were generated in the form of an orthogonal and sectional projection. Then, the 3D model was built. In Figure 1, the disassembled burner is shown with its parts. Only the necessary parts of the following CFD model have been introduced in the CAD.

Figure 1. The double impulse burner disassembled.

The perforated element of the inner part is called the internal barrel. The internal barrel can be crossed by the flow, both internally and externally. To adjust the flow distribution between inside and outside channels, there is a swab and a counter swab. The swab consists of a truncated cone, visible in Figure 2a, while the counter-swab is its counterpart. The

counter swab is rigidly constrained to the internal barrel; therefore, it can only be moved rigidly with it. Another fundamental element is the external nozzle, which is connected to the shroud with a threaded connection. The natural gas supply duct is above and inclined to ease the flow entrance through the internal channels.

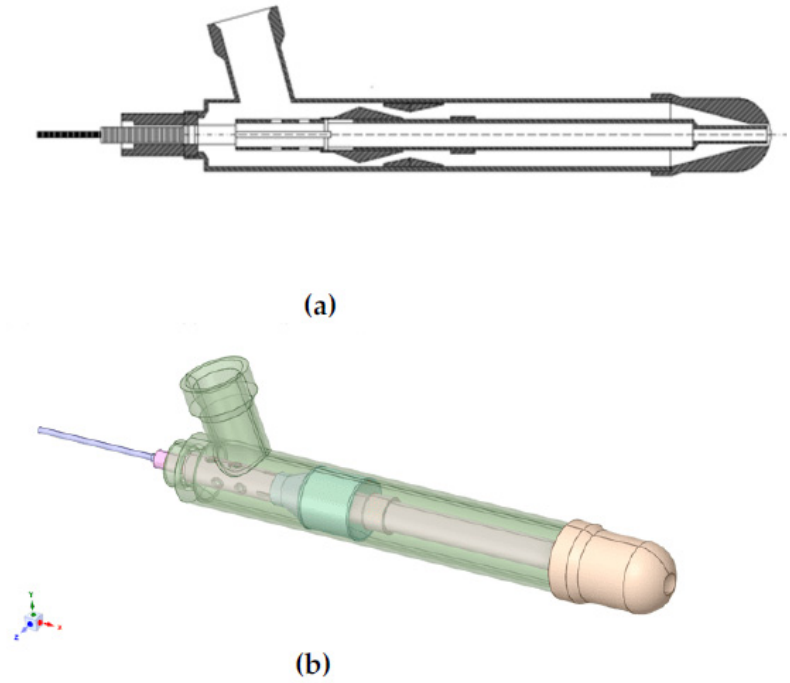

Figure 2. Reconstruction of the double impulse burner: (**a**) 2D section in a middle plane of the burner; (**b**) view of the 3D model.

The burner operation has three independent degrees of freedom. The shift of the burner parts related to the degrees of freedom is visible in Figure 3. The first is the axial shift of the swab. The swab, moving axially, occludes the annular section and limits the flow portion outside the barrel. In an extreme case, when the section is completely closed, the fluid can only flow in the inner channel. This degree of freedom will be referred to as Xswab. The second one is the axial shift of the internal barrel. The inner barrel can move axially to reach the outer nozzle section. This operation changes the mixing section between the internal and external flow. This degree of freedom will be referred to as Xbarrel. The last one is the total pressure value of the natural gas at the supply duct, called Ptot.

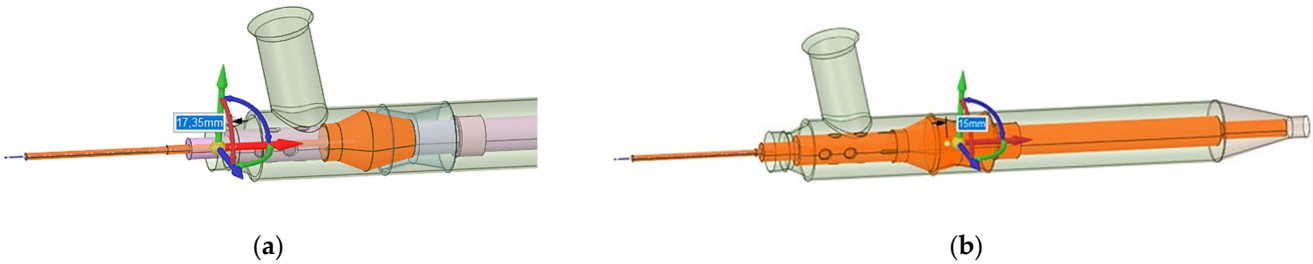

Figure 3. Degrees of freedom of the double impulse burner: (**a**) axial shift of the swab; (**b**) axial shift of the barrel.

3. CFD Model

To set up a CFD model able to correctly simulate the jet mixing process, a reference test case from literature has been used [13]. The reference paper also includes a series of experimental data for comparison with the numerical results. Furthermore, a case with multiple chemical species is analyzed; air in the outer (annular) duct and a mixture of He

and CO_2 in the inner one. Figure 4 shows an image of the geometry with two ducts, while Table 1 reports data from the three simulated cases.

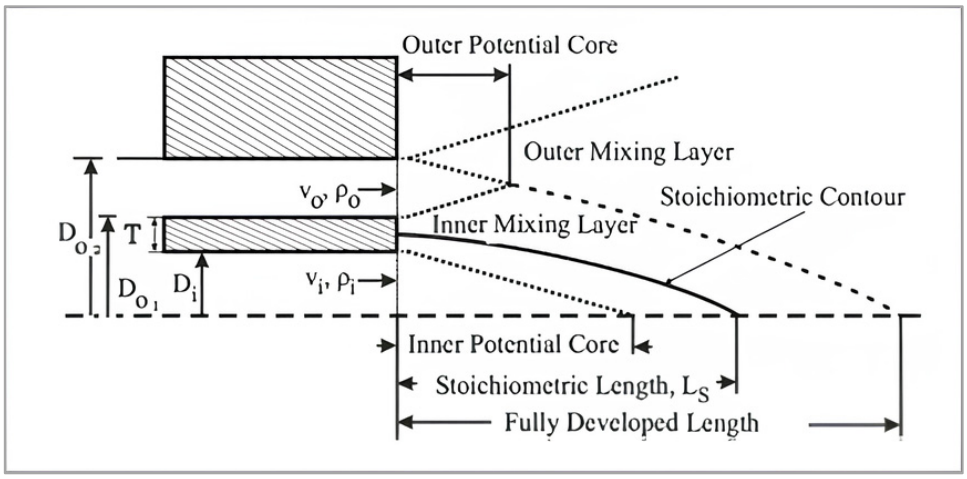

Figure 4. Image of the ducts in the literature case.

Table 1. Fluid properties used for test case simulations.

Test	$Fluid_i$	$Fluid_o$	D_h/D_i	T/D_i	V_r	D_r	M_r	Re_t	Re_o
B1	He-CO_2	Air	2.63	0.44	0.21	1.44	0.06	3.5	2.3
B2	He-CO_2	Air	2.63	0.44	0.42	1.44	0.25	3.5	4.65
B3	He-CO_2	Air	2.63	0.44	0.83	1.44	1.00	3.5	9.20

where: $V_r = V_o/V_i$: velocity ratio; $D_r = \rho o/\rho i$: density ratio; $M_r = D_r \cdot V_r^2$: momentum ratio; $D_h = D_{o2} - D_{o1}$ hydraulic diameter.

The selected tests are B1, B2, and B3 because they involve air as the secondary fluid for the mainstream outside the burner.

3.1. CFD Model Equations

The tests are performed using the Finite Volume Method code Ansys CFX, which involves a cell-vertex formulation. The problem involves incompressible fluid, and it is closed by the k-ω SST equation for turbulence. So, the equations solved in this formulation are:

Continuity equation with the incompressible and 2D formulation:

$$\frac{\partial u}{\partial x} + \frac{\partial v}{\partial y} = 0, \tag{1}$$

Momentum equations in x and y directions, in the 2D form:

$$\frac{\partial(\rho u)}{\partial t} + \frac{\partial \rho u u}{\partial x} + \frac{\partial \rho u v}{\partial y} = -\frac{\partial p}{\partial x} + \mu\left(\frac{\partial^2 u}{\partial x^2} + \frac{\partial^2 u}{\partial x \partial y}\right) + S_{Mx}, \tag{2}$$

$$\frac{\partial(\rho v)}{\partial t} + \frac{\partial \rho v u}{\partial x} + \frac{\partial \rho v v}{\partial y} = -\frac{\partial p}{\partial y} + \mu\left(\frac{\partial^2 v}{\partial x \partial y} + \frac{\partial^2 v}{\partial y^2}\right) + S_{My}, \tag{3}$$

The energy equation is written in terms of internal energy because we used the thermal energy option in Ansys CFX:

$$\frac{\partial(\rho i)}{\partial t} + \frac{\partial \rho i u}{\partial x} + \frac{\partial \rho i v}{\partial y} = -p\left(\frac{\partial u}{\partial x} + \frac{\partial v}{\partial y}\right) + k\left(\frac{\partial^2 T}{\partial x^2} + \frac{\partial^2 T}{\partial y^2}\right) + \xi + S_i, \tag{4}$$

where S_{Mx}, S_{My} and S_i are the source term for the different equations that, for our problem, are equal to 0, and ξ is the viscous dissipation term, not included in the options of the code since it needs a very fine mesh to resolve it. The fluid domain is composed of a mixture that involves CO_2, He, and air, so we need to specify a transport equation for CO_2 and He that, in the general form, is:

$$\frac{\partial(\phi_i)}{\partial t} + \nabla\cdot(\phi_i \vec{U}) = \nabla\cdot(\rho D_\phi \nabla\varphi_i) + S_\varphi, \tag{5}$$

where ϕ_i is the conserved quantity per unit volume of the different species, while φ_i is the conserved quantity per unit mass.

In order to solve the turbulence effect, we chose to use the SST k-ω model [20], which is a two equations model that involves a conservation equation for k and ω, written in a vectorial form as:

$$\frac{\partial k}{\partial t} + U_j\frac{\partial k}{\partial x_j} = P_k - \beta^* k\omega + \frac{\partial}{\partial x_j}\left[(\nu + \sigma_k\nu_T)\frac{\partial k}{\partial x_j}\right], \tag{6}$$

$$\frac{\partial \omega}{\partial t} + U_j\frac{\partial \omega}{\partial x_j} = \alpha S^2 - \beta\omega^2 + \frac{\partial}{\partial x_j}\left[(\nu + \sigma_\omega\nu_T)\frac{\partial \omega}{\partial x_j}\right] + 2(1-F_1)\sigma_{\omega 2}\frac{1}{\omega}\frac{\partial k}{\partial x_i}\frac{\partial \omega}{\partial x_i}, \tag{7}$$

This turbulence model has been used, for the same field of study, in Refs. [21,22]. Constants of the SST k-ω are set by CFX default.

3.2. CFD Model Validation

An unstructured mesh with 450,000 elements has been generated with Ansys Meshing, which is the result of a grid dependency study. In Figure 5, we present the mesh we used for this validation, showing local refinements on the walls for boundary layer solutions (prism layers) and in the interesting fluid areas, using mesh densities.

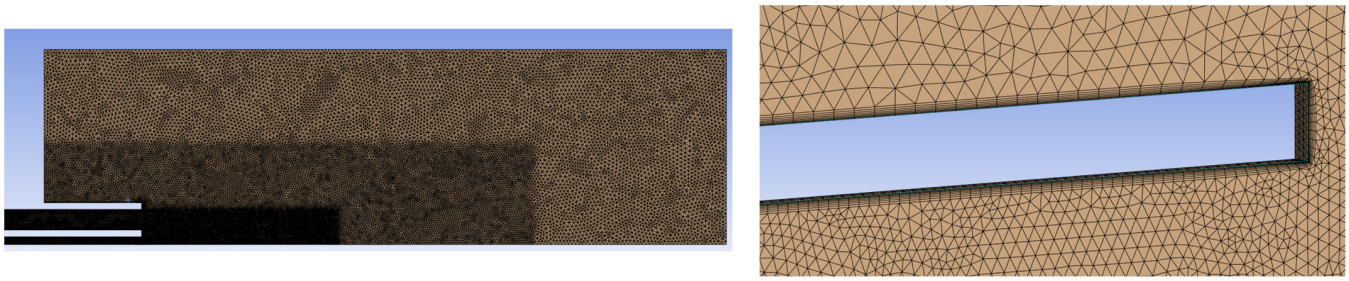

(**a**) (**b**)

Figure 5. Unstructured mesh used to reproduce the literature case: (**a**) View of the local refinements due to the volumes of densities; (**b**) Zoom on the walls of the ducts where the prism layers are present.

Steady flow solutions are performed. Fluids are considered to enter the ducts with a medium turbulence intensity (5%). The turbulence model was the SST (Shear Stress Transport) and the energy equation in Thermal Energy mode solving for internal energy. The gas is considered ideal and enters at 25 °C. The boundary conditions set are summarized in Figure 6.

A maximum number of iterations equal to 1000 is more than adequate to guarantee full iterative convergence. A mesh independency study has been performed for this model, with three different meshes: 500 thousand, 430 thousand, and 250 thousand elements. The results of the grid tests are shown in Table 2.

From the above results, the medium-refined mesh of 430 k elements has been selected. The results of the velocity at a fixed axial non-dimensional distance from the nozzle outlet of cases B1, B2, and B3 are presented in Figure 7.

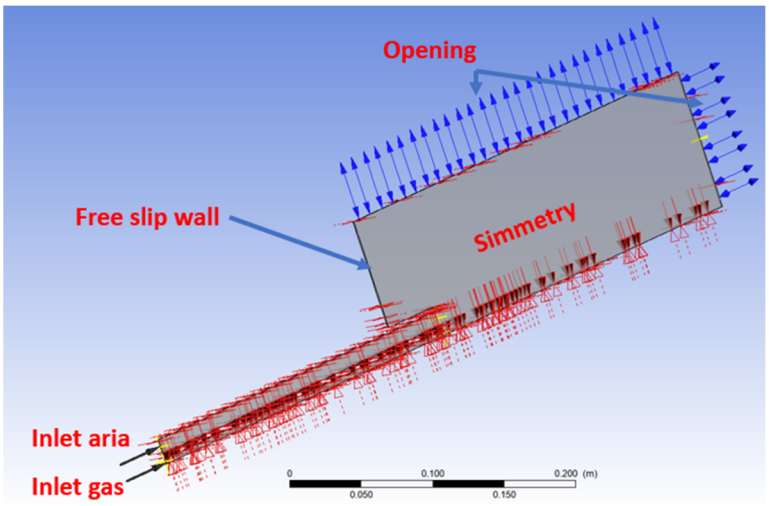

Figure 6. Boundary conditions set for the fluid domain.

Table 2. Mesh independence results.

N Elements	Average Velocity Internal Outlet [m/s]	Average Velocity External Outlet [m/s]	CO_2 Average Concentration at Internal Outlet	He Average Concentration at Internal Outlet
500 k	8.94	1.75	0.59	0.40
430 k	8.95	1.74	0.59	0.40
250 k	8.93	1.74	0.59	0.40

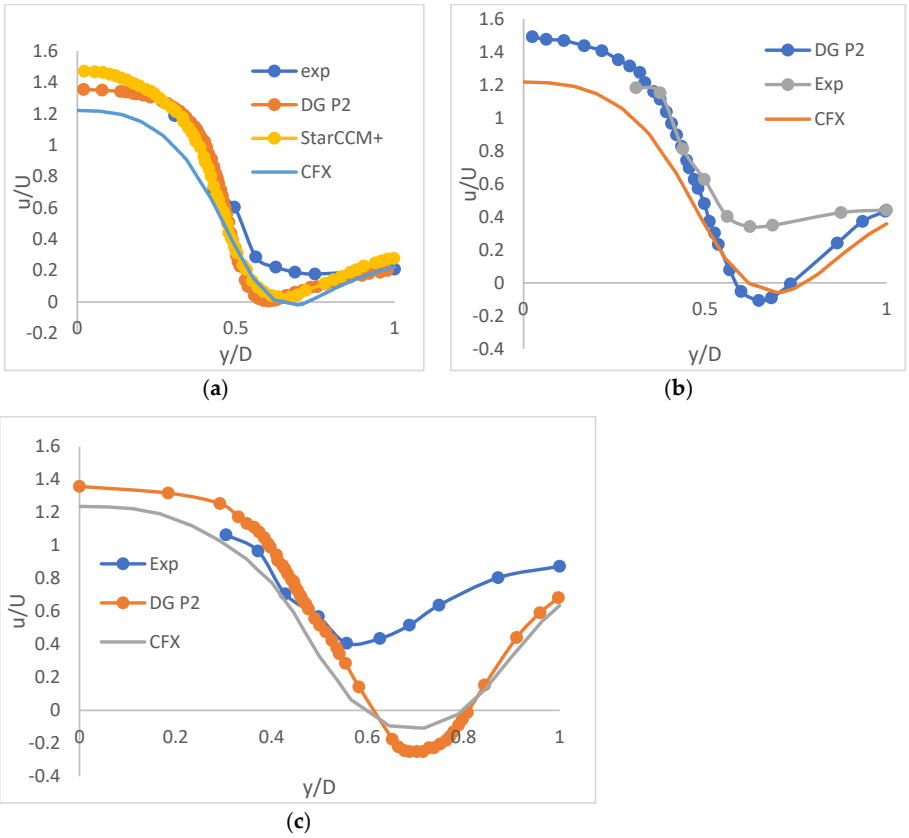

Figure 7. Dimensionless axial velocity graphs at dimensionless position x/D = 0.7: (**a**) Case B1; (**b**) Case B2; (**c**) Case B3.

Figure 7 shows the distribution of dimensionless u-component of velocity in cases B1, B2, and B3 at a dimensionless position of $\frac{x}{D} = 0.7$. The results of numerical simulations using Ansys CFX have been reported in comparison with other numerical codes and with experimental results. In the legend, DG P2 is the Discontinuous Galerkin finite element code used in [1] that claims up to third-order numerical accuracy. The CFX results slightly underestimates the value of the u-component of velocity with respect to experimental results. The overall trend of the profile follows the behavior of the other numerical codes for the three cases. Increasing the velocity ratio from B1 to B3 increases the separation zone and the entrainment effect towards the outlet of the external domain. From the above comparison, it can be concluded that the simulation approach is able to accurately reproduce the velocity profiles in all three cases when compared to the numerical and experimental reference data.

3.3. Double Impulse Burner CFD Model

After validating the model, it was possible to apply it to the case of the burner. Some geometric modifications have been made with respect to the mechanical drawing presented in Section 2. All external metal shims have been removed, as they are useless for CFD purposes. The outer casing was cut in correspondence with the counter swab, as it is assumed that there is a perfect fluid dynamic seal. Furthermore, the natural gas feed pipe was lengthened so that the fluid reaches the burner with a certain boundary layer development (more realistic). A fluid volume was created downstream of the nozzle outlet to analyze jet mixing.

The fluid has been set up as a mixture of methane and air, both of which are regarded as ideal gases. The presence of only methane entering the burner and only air in the fluid volume downstream of the nozzle was then specified in the boundary conditions. Methane with total inlet pressure was set as the inlet condition; its absolute value depends on the single case analyzed. The turbulence model used was the SST (Shear Stress Transport); the inlet methane temperature was equal to 15 °C (normal conditions), while the air was considered at 25 °C, and the heat exchange model was thermal energy. Opening conditions were set along the side walls of the duct, while no-slip wall conditions were set to the atmospheric volume wall in contact with the burner nozzle. The fluid domain is extended at the burner exit with an atmospheric volume where reference atmospheric pressure is set along with the opening boundary condition on the external surface. The set of boundary conditions is summarized in Figure 8.

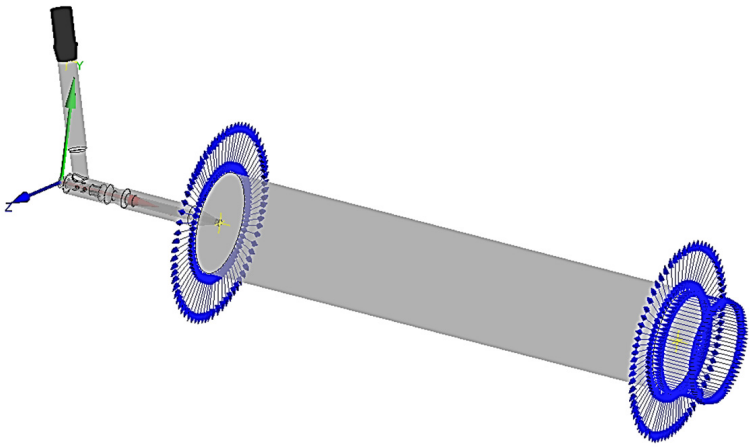

Figure 8. Boundary conditions are summarized in a screen where the two ducts (inner and outer) and the mixing fluid volume are present.

4. CFD Simulation

The first step was to simulate the burner with some configuration named “Case 0” that corresponds to the maximum opening of the two coaxial internal channels. An unstructured

mesh of about 20 million cells was generated with local refinements added on the wall and in specific fluid areas using mesh densities. Prism layers have been created along the walls. Some mesh images are presented in Figure 9, together with the control surfaces where the flow rates of the two coaxial channels are calculated.

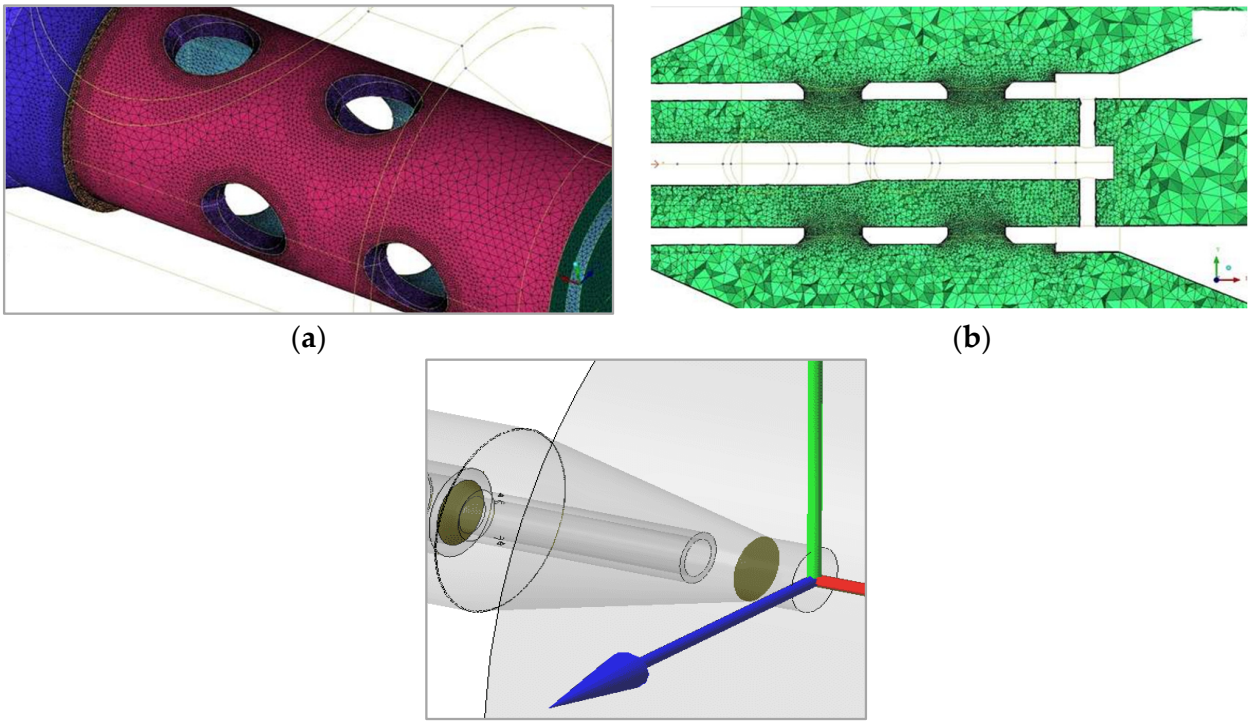

Figure 9. Images of the mesh: (**a**) Surface mesh on the internal barrel in correspondence with the holes through which the methane enters the internal barrel; (**b**) volume mesh seen in the midplane; (**c**) the control surfaces where the internal flow rate (on the left) and the total flow rate (on the right) have been calculated, blue arrow is for *z*-axis, red arrow is for *x*-axis and green arrow is for *y*-axis.

The inlet total pressure value is fixed with a flow direction normal to the inlet patch, and the reference atmospheric pressure is set in the external volume, where the flow is discharged. The flow structure of the outlet jet can be investigated using different post-processing methods, using contours of, for example, the Mach number at the mid-plane. A more detailed analysis uses a set of control planes at increasing distance from the burner exit (axial distance x normalized with the burner outlet diameter D, x/D) and plots the axial velocity profiles along the vertical lines as sketched in Figure 10.

The maximum Mach number in this configuration remains at subsonic levels, and the maximum velocities are at the outlet of the external nozzle and the end of the barrel. The velocity profiles, on the other hand, show a uniform maximum velocity in the central part of the jet and a tendency to expand radially, moving far from the outlet. In Figure 10b, only the axial component is shown since it was verified that the radial component of the velocity has very small values, mainly due to the radial jet expansion and the external air entrainment. The U-component of the velocity is normalized with the inlet velocity of the fluid. Using the control surfaces highlighted in Figure 9c, the distribution of the flow rates was calculated; the external channel value was obtained by the difference between the total and internal flow rate values. In this burner configuration, the mass flow repartition is 20.6% in the inner channel and the remaining 79.4% in the outer coaxial channel. Case 0 has been used to set up the whole simulation process that will be systematically applied to each case from the DOE database.

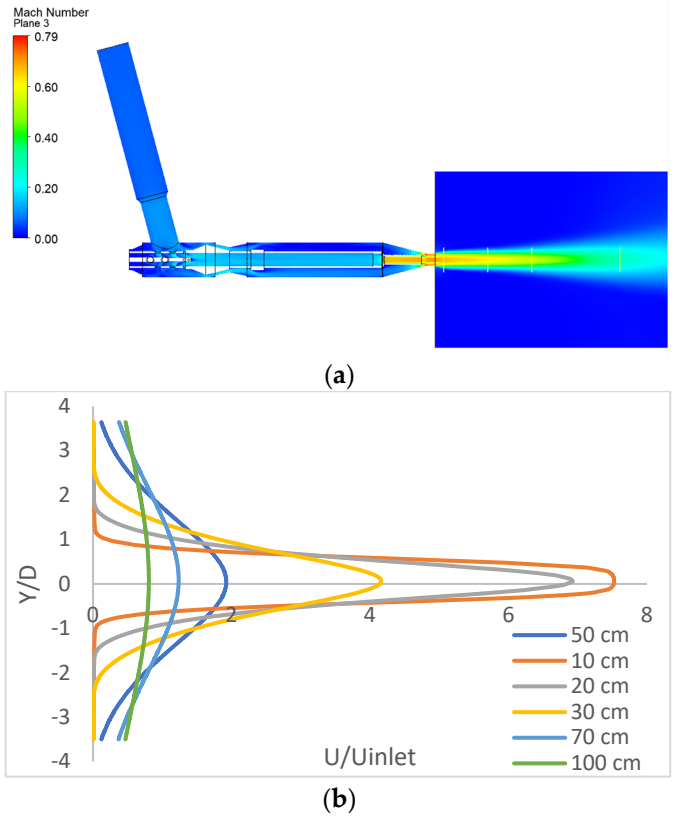

Figure 10. (**a**) Mach number contour on the burner midplane; (**b**) Axial velocity profile along lines at increasing normalized distance x/D from the burner exit.

5. Surrogate Model of the Double Impulse Burner

A surrogate model is an engineering method used when an outcome of interest cannot be easily measured or computed, so a mathematical model of the output is considered. Most problems require experiments and/or simulations to evaluate design objectives and constraint functions as a function of design variables. The major challenge of surrogate modeling is the generation of a model that is as accurate as possible, using few simulations. The surrogate model process is divided into three main steps:

- Selection of Samples (using DOE techniques)
- Construction of the surrogate model and optimization of variable parameters
- Evaluation of the surrogate model accuracy

The most frequent surrogate models are polynomial response surfaces, kriging, Bayesian approaches, radial basis functions, artificial neural networks, and Bayesian networks. The Latin Hypercube method has been selected as the DOE technique, and Artificial Neural Network as the main surrogate model. A database of simulations with different geometric configurations and different total inlet pressure has been generated and used to train and tune the metamodels for the mass flow rate repartition and the outlet velocity profile. The first step is to generate a population of different combinations of the three input variables (two geometrical and the inlet gas total pressure) that need to be simulated with the CFD model to attain the output quantities of interest (mass flow rates repartition and velocity profile) to be modeled with a surrogate approach. To have a good filling of the overall design space with a limited number of individuals, the population of configurations has been generated using a DOE technique as in the following.

5.1. Design of Experiments (DOE)

The Latin Hypercube algorithm to generate a DOE using the Dakota software platform [23] has been selected. Latin hypercube sampling (LHS) is a statistical method for generating

a near-random sample of parameter values from a multi-dimensional distribution. In statistical sampling, a square grid containing sample positions is a Latin square if there is only one sample in each row and each column. A Latin hypercube is the generalization of this concept to an arbitrary number of dimensions, where each sample is the only one in each axis-aligned hyperplane containing it. The design space is subdivided into an orthogonal grid with N elements of the same length for parameters. In multi-dimensional DOE, N-sub volumes are built so that along each row and each column of the grid, only one sub-volume is chosen. Inside each sub-volume, a sample is randomly chosen. The range of variation of each independent variable and the number of individuals has been defined. From previous experience [24,25], thirty-two cases have been considered acceptable with only three independent variables. Figure 11 shows a graphical representation of the DOE in 3D. The independent variables are normalized in the range [0, 1].

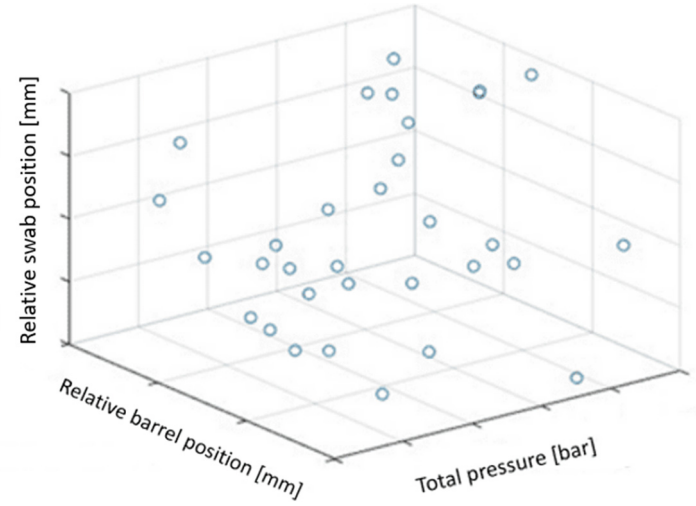

Figure 11. Graphic representation of the design space. The points in the figure represent the thirty-two configurations of the database.

For each case of the DOE, the geometry was adapted from the 3D CAD model, a new mesh was produced, and a new CFD simulation was performed. The purpose of this simulation campaign was to obtain a series of data regarding the flow rate and its distribution and the output velocity profiles. Using the post-processed data from the CFD simulations, the surrogate models have been developed as described in the following paragraphs.

5.2. Response Surface Method for Mass Flow Rate Repartition

A response surface is a function of the type:

$$y = f(x_1, x_2 \ldots x_n) \tag{8}$$

The industrial interest is the knowledge of the total flow rate and its repartition inside the burner from the degrees of freedom of the problem. The following functions were then produced for the total mass flow and the internal one:

$$\dot{m}_{tot} = f(X_{barrel}, X_{swab}, P_{tot}) \tag{9}$$

$$\dot{m}_{int} = f(X_{barrel}, X_{swab}, P_{tot}) \tag{10}$$

The mass flow in the external coaxial channel is obtained as a difference. These relationships were obtained using the Artificial Neural Network algorithm using the Dakota software. The matrix containing all the results of the mass flow rates and the relative positions of the barrel, swab, and the inlet total pressure is used to train and test the surrogate models. This matrix is composed of the CFD results for the mass flow rates in one

column, that is, the function output, and in the other three columns, there are the degrees of freedom of the problem, meaning X_{barrel}, X_{swab}, and P_{tot}. These variables are used in the Dakota software to obtain a response function using the Artificial Neural Network method, obtaining a hyperbolic tangent-type function that relates the mass flow results to the geometrical configuration of the single case and the inlet total pressure. In order to evaluate the efficiency of the Artificial Neural Network, we decided to use different types of solutions. First, we used the first half of the cases to train the network and the second half to test it. Then, we inverted the method and used the second half of the results to train the network and the first half to test it. Afterward, we selected cases from 1 to 26 to train the network and cases 27 to 32 to test it. For the last try, we used cases 7 to 32 to train the network and 1 to 6 to test it. The results were compared in terms of average percentage error between the results of the network and the CFD results, and the best results were given by the last methodology, where the average percentage error was about 6% compared to the CFD results. The definition of the average percentage error is given by Equation (11) below. This function has been tested compared to numerical results. The above functions cannot be represented in 3D space; to draw the response surfaces, it was decided to fix five different total inlet pressure values and produce parametric graphs with the other two geometrical input variables, as shown in Figure 12.

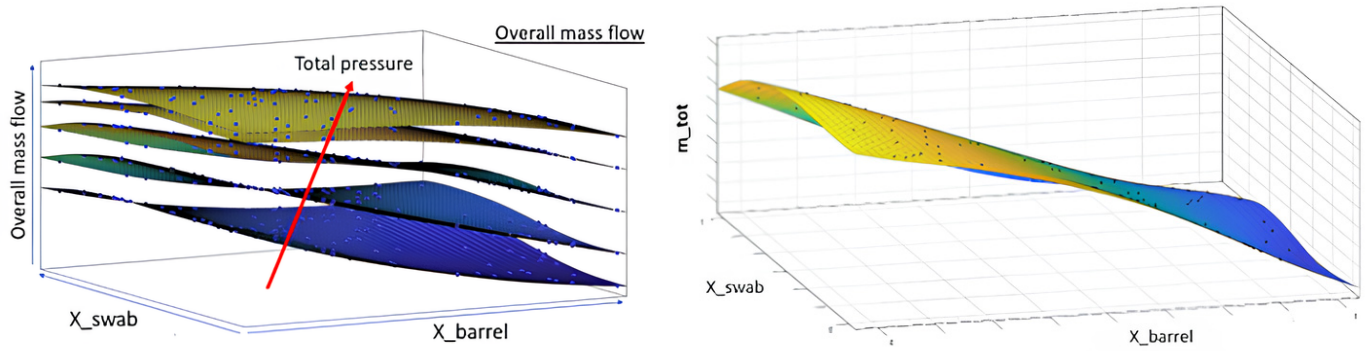

(**a**) (**b**)

Figure 12. Response surface graphs: (**a**) total mass flow versus barrel and swab positions for five different total pressure levels; (**b**) graph of the response surface for the total flow rate as the barrel and swab positions vary for an intermediate total pressure value.

A strong dependence, as expected, of the total pressure on the maximum flow rate is observed. Focusing on Figure 12b, to attain the dependence on the other two free parameters, a decrease in the flow rate as the barrel advances are observed. The total mass flow rate in Figure 12b is higher where there is a yellow color, instead of the blue color that represent a lower mass flow rate; it is due to the restriction that this causes in the internal section of the external channel. The dependence of the position of the swab on the internal flow rate is generally less marked and becomes relevant when it reaches the closure of the annular section. The position of the internal part has a non-negligible effect on the overall pressure drops of the burner and, therefore, on the total mass flow rate. A similar analysis can also be performed for the mass flow into the internal channel from Figure 13.

The internal flow rate also has a strong link with the total inlet pressure. However, from Figure 13b, a strong influence from the position of the internal barrel (that generates the contraction of the final part of the nozzle) is detected. An higher internal mass flow is represented by yellow color in Figure 13b, where blue color represent lower mass flow; it behaves similarly to a second pressure drop in series with that of the swab and counter-swab mechanism. On the other hand, it is observed that the swab seems to have an overall limited influence. It is evident that the overall closing of the swab would result in the flow stream into the internal section only. For reasons related to the construction of the mesh, it was not possible to simulate situations very close to the maximum axial position since the remaining annular section would have been too small; therefore, $X_{swab} = 1$ does not

correspond in our case to the complete closure of the annular section. It is nevertheless clear that the axial position of the swab has a relevant importance when it comes very close to this condition since, as can be clearly seen from the image, it appears to have a limited influence far from this condition. To test the functions obtained through the ANN response surfaces, the flow rates from the surrogate models were compared to those from the CFD results. In Figure 14, the relative percentage error and the frequency it occurs in the dataset are shown.

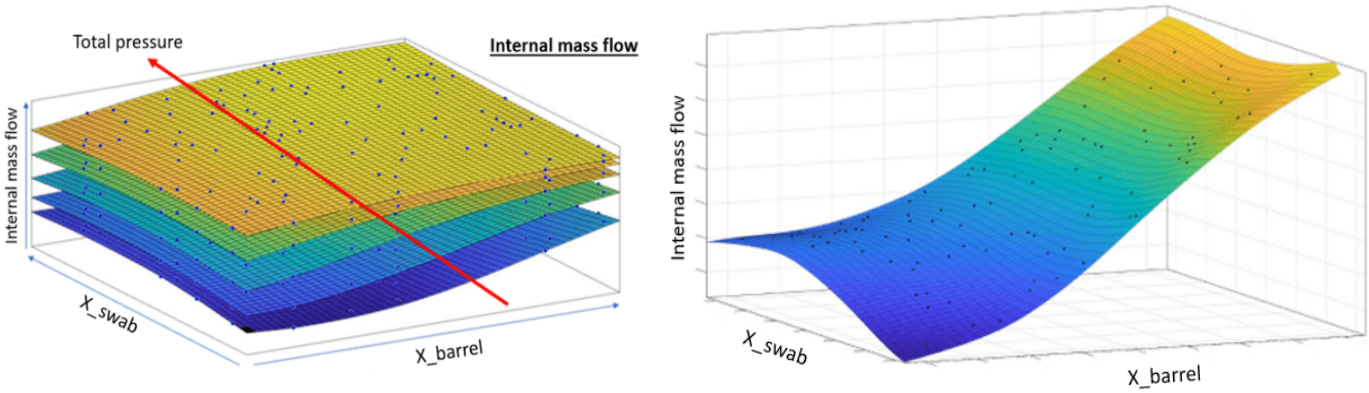

(**a**) (**b**)

Figure 13. Graphical representation of response surfaces for mass flow into the internal channel. (**a**) parameterization of the function for five different total pressure values (**b**) trend of the internal flow rate as the axial positions of the barrel and swab vary for an intermediate total pressure level.

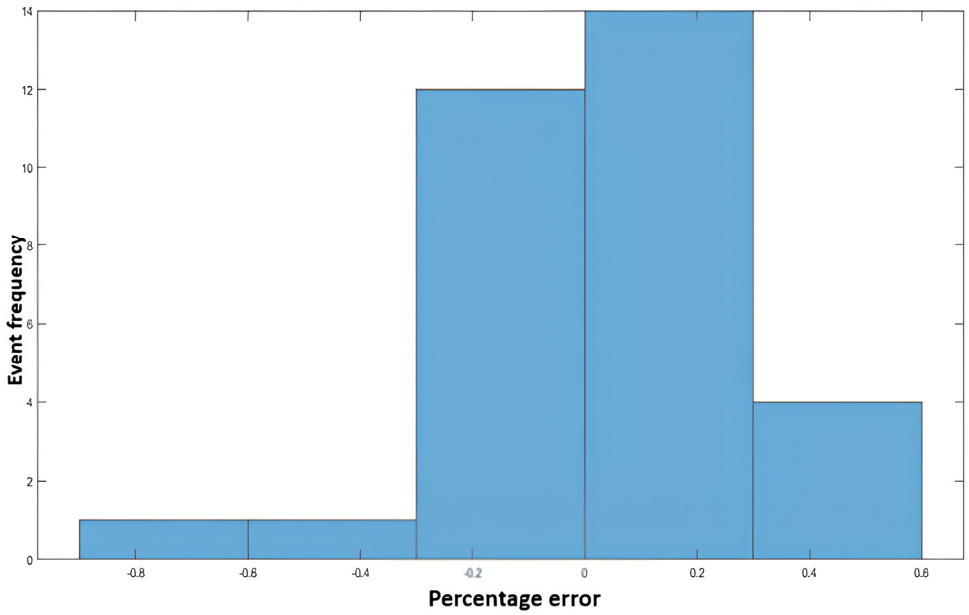

Figure 14. Errors between surrogate models and CFD values. On the *x*-axis the error, on the y-axis the number of times the error occurred.

The relative percentage error is defined as:

$$Percentage\ error = 100 \cdot \frac{\dot{m}_{CFD} - \dot{m}_{ANN}}{\dot{m}_{CFD}} \tag{11}$$

An absolute maximum value of 0.9% is obtained, demonstrating the good accuracy of the surrogate models.

5.3. Response Surface Method for Dimensionless Velocity Profiles

The velocity profiles at different distances from the outlet have been obtained from the dataset of CFD simulations. The objective of the work was to be able to model the velocity profile from the three input variables related to burner setting and inlet gas total pressure. The different profiles were first analyzed at the nozzle outlet section (x/D = 0); these are shown in Figure 15, where there is an image of some profiles at the outlet. The velocity profiles are made non-dimensional with the average value of the maximum value obtained in the different solutions.

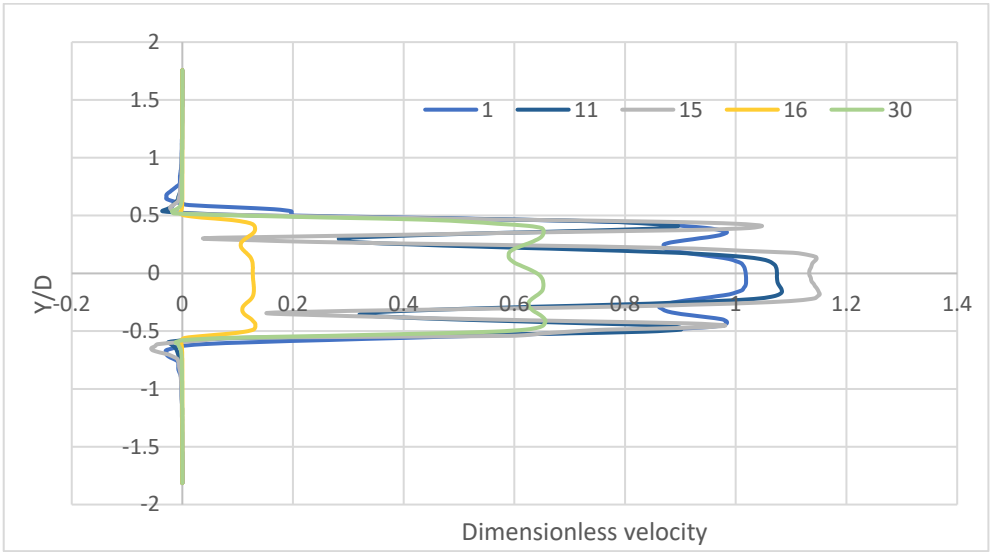

Figure 15. Dimensionless velocity at the outlet (x/D = 0) for some DOE cases.

At the burner outlet section, the profiles are very different from each other and with a shape that would be very difficult to model. Considering that the diffusive flame reaction will never develop at the burner exit section (installed at the wall furnace), the profiles at an axial distance equal to x/D = 0.7 have been considered; they are shown in Figure 16a in non-dimensional form.

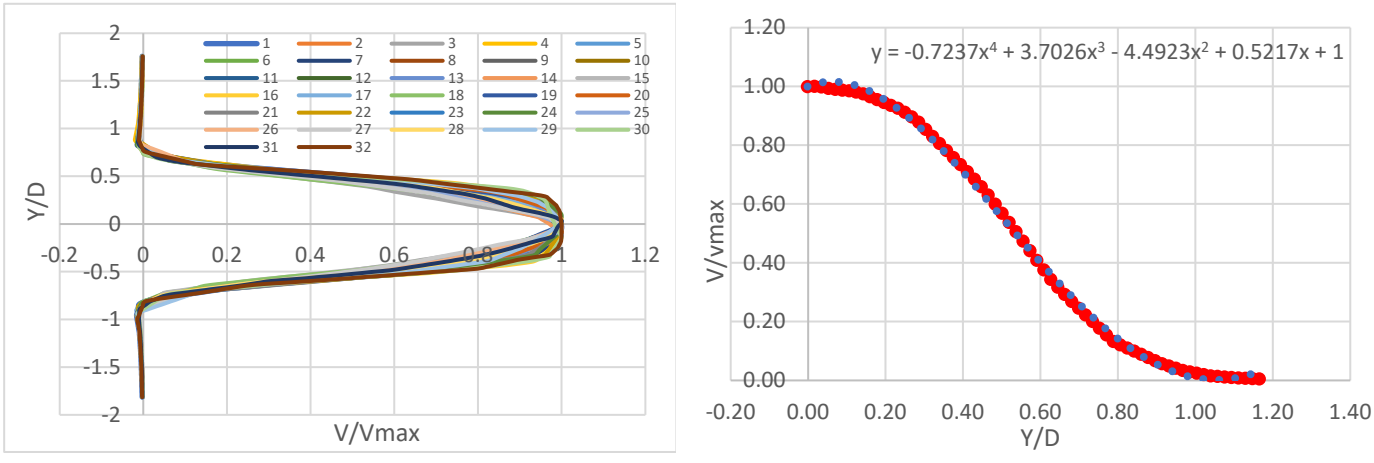

(**a**) (**b**)

Figure 16. Dimensionless velocity profiles at x/D = 0.7: (**a**) Dimensionless speed profiles with their own maximum speed value and all reported on the same graph: (**b**) Example of a fourth-order polynomial least squares regression; red dot is the calculated profile, blue dot is the reconstructed profile.

Each profile was regressed using Matlab software with the poly fit routine, which performs a least squares regression. A fourth-order polynomial regression turned out to be

the most accurate to model all the profiles in the dataset. The regression function has the following form:

$$\frac{V_i}{V_{max,i}} = a_i \times \left(\frac{y}{D}\right)^4 + b_i \times \left(\frac{y}{D}\right)^3 + c_i \times \left(\frac{y}{D}\right)^2 + d_i \times \left(\frac{y}{D}\right) + 1 \quad (12)$$

For every profile, the four coefficients a_i, b_i, c_i, and the corresponding $V_{max,i}$ need to be modeled as a function of the three input variables, using appropriate response surfaces. In this case, the cubic polynomial fit had the best response surface algorithm. To test the accuracy of the reconstructed profiles, they were compared with those from CFD simulations, as shown in Figure 17, with minimal differences. To quantify the error introduced by the modeled velocity profile, the corresponding integral mass flow rate has been compared to the reference value from the CFD simulation.

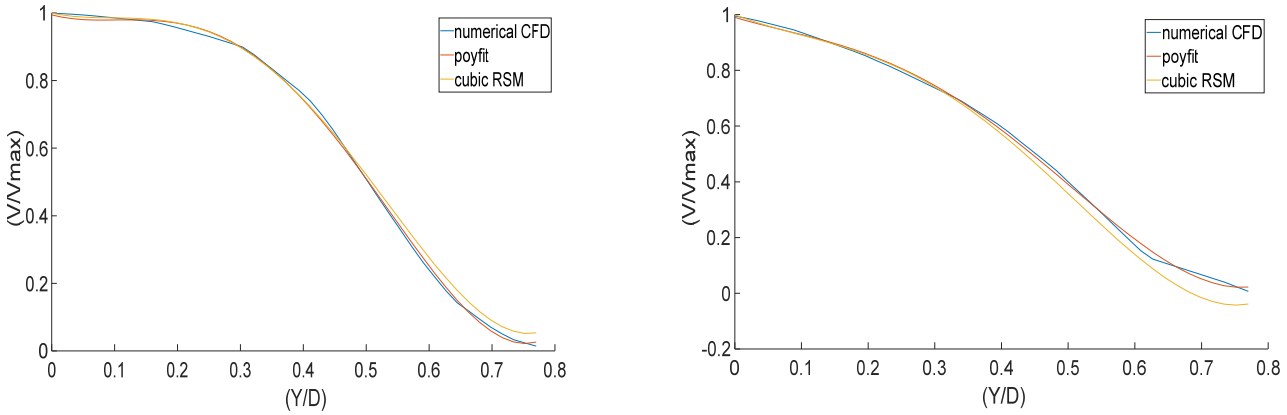

Figure 17. Screenshot of the test file on velocity profiles: (**a**) example of a "squared" speed profile; (**b**) example of a "sharp" speed profile.

The integral mass flow rate from the profile is calculated using the equation:

$$\dot{m} = 2\pi\rho V_{max} \int_0^R V(r) \times r \, dr \quad (13)$$

where R is the radius where the axial velocity is equal to zero, in all cases, the error on the mass flow rate is less than 3%.

6. Conclusions

Starting from the original burner geometry, thirty-two configurations were obtained from a Latin Hypercube DOE and simulated using a CFD model. The results were used as a basis for generating response surfaces for the mass flow rate repartition inside the two coaxial channels and for the velocity profile at the burner exit. The above models are useful both to support the operation setting of the burner in the industrial environment and to give a reliable boundary condition to the CFD reactive simulation of the diffusive flame in the furnace. A database of simulations with different geometric configurations and different total inlet pressure has been generated and used to train and tune the metamodels for the mass flow rate repartition and the outlet velocity profile. Results show a strong dependence, as expected, of the total pressure on the maximum flow rate. In addition, a decrease in the maximum flow rate as the barrel advances is observed due to the passage area reduction caused in the inner section of the external channel. The internal mass flow rate is also affected by the inlet total pressure, but the main influence on this parameter is the internal barrel position. The swab position has a limited influence on the internal mass flow rate unless it reaches its maximum relative position when it derives a complete blockage of the external channel. Numerical results have been used to generate a response surface using

an Artificial Neural Network algorithm; this response surface has been interrogated to show that the percentage error between the numerical approach and the response surface approach is low, and the response surface can be used to obtain results in many different geometrical solutions with negligible computational time. The response surface method has also been used to model the velocity profile outside the burner. Each profile was regressed using Matlab software with the poly fit routine that performs a least squares regression. A fourth-order polynomial regression turned out to be the most accurate to model all the profiles in the dataset. Results have been tested from the integral mass flow rate point of view; comparison showed that the percentage error is less than 3% in all cases. The modeling approach presented can be applied to other configurations of burners, and it is considered a valuable tool to have representative input data for the combustion simulations inside the furnace necessary for the prediction of diffusive flames. The accurate prediction of the diffusive flame strictly depends on the velocity profile of the fuel gas that has a direct influence on the air-fuel mixing processes and combustion development. To be accurate in energy consumption and pollutant formation, which are the current primary challenges for the glass industry, the right velocity profile from the fuel injection is of utmost importance. It has not been detailed for a double impulse industrial burner in no other public sources.

Author Contributions: Conceptualization, C.C., A.L. and L.P.; Methodology, C.C., A.L. and L.P.; Software, C.C., A.L. and L.P.; Validation, C.C., A.L. and L.P.; Formal analysis, C.C., A.L. and L.P.; Investigation, C.C., A.L. and L.P.; Resources, C.C., A.L. and L.P.; Data curation, C.C., A.L. and L.P.; Writing—original draft, C.C., A.L. and L.P.; Writing—review & editing, C.C., A.L. and L.P.; Visualization, C.C., A.L. and L.P.; Supervision, C.C. and A.L.; Project administration, C.C.; Funding acquisition, C.C. All authors have read and agreed to the published version of the manuscript.

Funding: This research received no external funding.

Data Availability Statement: No new data were created or analyzed in this study. Data sharing is not applicable to this article.

Acknowledgments: The authors are grateful for the support provided by Bormioli Rocco S.p.A., that has provided the original geometry of the industrial burner used for calculations and supplied technical and operative support.

Conflicts of Interest: The authors declare no conflict of interest.

References

1. Simpson, N. Burners for glass melting furnaces. *Environ. Sci.* **2007**, *60*, 73–77.
2. Korstanje, L.J.; Martin, P. Studies on High Temperature Low Nox Combustion for Glass Furnaces. In Proceedings of the Institute of Energy's Second International Conference on Combustion & Emissions Control, London, UK, 4–5 December 1995; pp. 295–307.
3. Nakamura, T.; Smart, J.P.; VandeKamp, V.L. The effects of fuel/air mixing on NOx reduction and heat-transfer in high-temperature gas-fired glass-melting furnaces. *J. Inst. Energy* **1996**, *69*, 39–50. [CrossRef]
4. Liu, B.; Bao, B.; Wang, Y.; Xu, H. Numerical simulation of flow, combustion and NO emission of a fuel- staged industrial gas burner. *J. Energy Inst.* **2017**, *90*, 441–451. [CrossRef]
5. Guihua, H.; Honggang, W.; Feng, Q. Numerical simulation on flow, combustion and heat transfer of ethylene cracking furnaces. *Chem. Eng. Sci.* **2011**, *66*, 1600–1611. [CrossRef]
6. Zhou, W.; Moyeda, D.; Payne, R.; Berg, M. Application of numerical simulation and full scale testing for modeling low NO_X burner emissions. *Combust. Theory Model.* **2009**, *13*, 1053–1070. [CrossRef]
7. Khazaei, A.K.; Hamidi, A.A.; Rahimi, M. Numerical Investigation of Fuel Dilution Effects on the Performance of the Conventional and the Highly Preheated and Diluted Air Combustion Furnaces. *Chin. J. Chem. Eng.* **2009**, *17*, 711–726. [CrossRef]
8. Abbasi, K.B.; Hamidi, A.A.; Rahimi, M. Numerical Modeling and Simulation of Highly Preheated and Diluted Air Com bustion Furnaces. *Int. J. Eng.* **2009**, *22*, 107–118.
9. Bao, M.; Lin, J. Numerical simulation of combustion distribution in a gas burner. In *E3S Web of Conferences*; EDP Sciences: Les Ulis, France, 2021; Volume 236, p. 01002.
10. Chen, S.; Xing, Y. CFD investigation on Low-NO_x strategy of folded flame pattern based on fuel-staging natural gas burner. *Appl. Therm. Eng.* **2017**, *112*, 1487–1496. [CrossRef]
11. Mei, S.; Xie, J.; Han, D. Numerical Simulation in Combustion Space of an Oil Fired Oxy-fuel Glass Furnace with Different Burner Arrangments. *Int. Conf. Comput. Intell. Softw. Eng.* **2009**, 1–4. [CrossRef]

12. Choudhary, M.K. Recent Advances in Mathematical Modeling of Flow and Heat Transfer Phenomena in Glass Furnaces. *J. Am. Ceram. Soc.* **2002**, *85*, 1030–1036. [CrossRef]
13. Franchina, N.; Savini, M.; Bassi, F. Numerical simulation of non-reacting fuel-air coaxial jets by means of a novel high-order method. *Comput. Fluids* **2021**, *216*, 104814. [CrossRef]
14. Villermaux, E.; Rehab, H. Mixing in Coaxial Jets. *J. Fluid Mech.* **2000**, *216*, 161–185. [CrossRef]
15. Behrouzi, P.; McGuirk, J.J. Experimental Studies of Coaxial Jet Flows. *J. Fluid Sci. Technol.* **2007**, *2*, 346–358. [CrossRef]
16. Khandelwal, B.; Lili, D.; Sethi, V. Design and study on performance of axial swirler for annular combustor by changing different design parameters. *J. Energy Inst.* **2014**, *87*, 372–382. [CrossRef]
17. Yang, W.; Blasiak, W. Numerical study of fuel temperature influence on single gas jet combustion in highly preheated and oxygen deficient air. *Energy* **2005**, *30*, 385–398. [CrossRef]
18. Falcitelli, M.; Pasini, S.; Tognotti, L. Modelling practical combustion systems and predicting NOx emissions with an integrated CFD based approach. *Comput. Chem. Eng.* **2002**, *26*, 1171–1183. [CrossRef]
19. Galletti, C.; Parente, A.; Tognotti, L. Numerical and experimental investigation of a mild combustion burner. *Combust. Flame* **2007**, *151*, 649–664. [CrossRef]
20. Menter, F.R. Two-equation eddy-viscosity turbulence models for engineering applications. *AIAA J.* **1994**, *32*, 1598–1605. [CrossRef]
21. Gaikwad, P.; Kulkarni, H.; Sreedhhara, S. Simplified numerical modelling of oxy-fuel combustion of pulverized coal in a swirl burner. *Appl. Therm. Eng.* **2017**, *124*, 734–745. [CrossRef]
22. Ghasemi, E.; Soleimani, S.; Lin, C.X. RANS simulation of methane-air burner using local extinction approach within eddy dissipation concept by OpenFOAM. *Int. Commun. Heat Mass Transf.* **2014**, *54*, 96–102. [CrossRef]
23. Dakota-Explore and Predict with Confidence. Available online: https://dakota.sandia.gov/ (accessed on 13 January 2023).
24. Cravero, C.; Macelloni, P.; Briasco, G. Three-dimensional design optimization of multi stage axial flow turbines using a RSM based approach. In Proceedings of the ASME Turbo Expo 2012: Turbine Technical Conference and Exposition, Copenhagen, Denmark, 11–15 June 2012.
25. Campora, U.; Cravero, C.; Zaccone, R. Marine Gas Turbine Monitoring and Diagnostics by Simulation and Pattern Recognition. *Int. J. Nav. Arch. Ocean Eng.* **2018**, *10*, 617–628. [CrossRef]